

Supporting Information

A Canted Antiferromagnetic Ordered Phase of Cyanido-Bridged Mn^{III}₂Re^{IV} Single-Chain Magnets

Indrani Bhowmick,^{a,b} Elizabeth A. Hillard,^{a,b} Pierre Dechambenoit,^{a,b} Claude Coulon,^{a,b} T. David Harris,^c and Rodolphe Clérac^{a,b,*}

^a CNRS, CRPP, UPR 8641, F-33600 Pessac, France. Fax: (+33) 5 56 84 56 00; Tel: (+33) 5 56 84 56 50; E-mail: clerac@crpp-bordeaux.cnrs.fr

^b Univ. Bordeaux, CRPP, UPR 8641, F-33600 Pessac, France.

^c Department of Chemistry, University of California, Berkeley, California 94720, USA.

Synthesis

All chemicals and solvents were reagent grade. $(\text{Bu}_4\text{N})_2[\text{ReCl}_4(\text{CN})_2] \cdot 2\text{DMA}$ and $[\text{Mn}^{\text{III}}(5\text{-Me-saltmen})(\text{H}_2\text{O})]_2(\text{ClO}_4)_2$ (5-Me-saltmen²⁻: *N,N'*-(1,1,2,2-tetramethylethylene)bis(5-methyl-salicylidene-iminate)) were synthesized according to literature methods.^{1,2} All the following procedures were carried out at room temperature. *Caution! Perchlorate salts are potentially explosive and should be handled in small quantity.*

[Mn^{III}(5-Me-saltmen)]₂[Re^{IV}Cl₄(CN)₂]•3CH₃CN (1): $[\text{Mn}^{\text{III}}(5\text{-Me-saltmen})(\text{H}_2\text{O})]_2(\text{ClO}_4)_2$ (10.4 mg, 0.0100 mmol) and 10.4 mg (0.0100 mmol) of $(\text{Bu}_4\text{N})_2[\text{Re}^{\text{IV}}\text{Cl}_4(\text{CN})_2] \cdot 2\text{DMA}$ were separately dissolved in 2 ml of acetonitrile. The solution of the Mn^{III} precursor was transferred to a 1.5 cm diameter thin tube and then layered with 2 ml of acetonitrile. On the top of the pure solvent, the solution of the Re^{IV} precursor was very carefully layered to avoid any mixing of the reactants. The tube was then sealed with paraffin to prevent solvent evaporation. After 2 days, brown crystalline needles formed at the bottom and walls of the tube. The crystals were collected by filtration and air-dried. An 85 % yield was reproducibly obtained based on the Mn^{III} precursor. Elemental analysis calcd (%) for C₅₂H₆₁Cl₄Mn₂N₉O₄Re ($M = 1313.98$ g/mol): C 47.53, H 4.68, N 9.59; and experimentally found (%) as C 47.28, H 4.75, N 9.50; IR (KBr): $\bar{\nu} = 2141$ (C≡N stretch), 1596 (C=N stretch) cm^{-1} .

[1] H. Miyasaka, R. Clérac, T. Ishii, H. Chang, S. Kitagawa, M. Yamashita, *J. Chem. Soc., Dalton Trans.* **2002**, 1528

[2] T. D. Harris, M. V. Bennett, R. Clérac, J. R. Long *J. Am. Chem. Soc.*, **2010**, 132, 3980.

Physical characterization: Elemental analyses (C, H, and N) were carried out by a FlashEATM 1112 automatic elemental analyzer. Infrared spectra were recorded from 400 to 4000 cm^{-1} on a Nicolet750 Magna-IR spectrometer using KBr pellets. Magnetic susceptibility measurements were obtained using a Quantum Design MPMS-XL SQUID magnetometer. The measurements were performed on a freshly filtered polycrystalline sample of **1** introduced in a polyethylene bag ($3 \times 0.5 \times 0.02$ cm). The *dc* measurements were conducted from 280 to 1.8 K and between -7 T and 7 T applied *dc* fields. An *M* vs *H* measurement was performed at 100 K to confirm the absence of ferromagnetic impurities. The field dependence of the magnetization was measured between 1.83 and 10 K with a *dc* magnetic field between -7 T and 7 T. The *ac* susceptibility experiments were performed at various frequencies ranging from 1 to 1500 Hz with an *ac* field amplitude of 3 Oe in zero *dc* field. Experimental data were corrected for the sample holder and for the diamagnetic contribution of the sample.

Single crystal X-ray diffraction: Crystallographic data were collected on a single crystal of **1** with a Nonius diffractometer Kappa CCD equipped with graphite monochromator centered on the path of MoK α ($\lambda = 0.71073$ Å). The single crystal was coated with Paratone N-oil and mounted on a fiber loop followed by data collection at 150 K. The program Denzo-MNCH was used to integrate the data after an absorption correction with SADABS [3]. The structure was solved by direct methods and refined by least squares on F² in SHELX97 [4]. All non-hydrogen atoms were refined anisotropically by full-matrix least-squares (SHELXL-97). All hydrogen atoms were placed using a riding model. Their positions were constrained relative to their parent atom using the appropriate HFIX command in SHELXL-97. In the

crystal structure of **1**, one acetonitrile molecule is disordered on two positions. Hydrogen atoms belonging to this acetonitrile molecule were not introduced in the crystal structure, but are taken into account in the compound formula. Table 1 contains the summary of the unit cell and structure refinement parameters. (The CIF file is found in supporting information).

[3] Sheldrick, G. M. SADABS, Version 2.03; Bruker Analytical X-Ray Systems, Madison, WI, 2000.

[4] Sheldrick, G. M. SHELXTL, Version 6.12; Bruker Analytical X-Ray Systems, Madison, WI, 2000

Table S1. Crystallographic parameters for **1**

Formula	C ₅₂ H ₆₁ Cl ₄ Mn ₂ N ₉ O ₄ Re
Molecular weight (g.mol ⁻¹)	1313.98
Crystal size	0.26 x 0.20 x 0.16 mm
Temperature (K)	150(2)
Wavelength	0.71073 Å
Crystal System	monoclinic
Space group	P21/c
a (Å), b (Å), c (Å)	11.53210(3), 17.45220(5), 14.08240(4)
β (°)	93.2088(18)
Volume (Å ³)	2829.788(14)
Z	2
Density (g.cm ⁻³)	1.542
μ (mm ⁻¹)	2.813
F000	1322
θ range for data collection	3.48 to 27.48°
Limiting indices	-14 ≤ h ≤ 14, -22 ≤ k ≤ 22, -18 ≤ l ≤ 18
Reflections collected / unique	12187 / 6435 [R(int) = 0.0404]
GooF	1.025
^a R ₁ , ^b wR ₂ (<i>I</i> > 2.00 σ(<i>I</i>))	0.0328, 0.0739
^a R ₁ , ^b wR ₂ (all reflections)	0.0506, 0.0807
Largest diff. peak and hole	1.286 and -0.943 e.Å ⁻³

a) R₁ = $\sum ||F_o| - |F_c|| / \sum |F_o|$.

b) wR₂ = $[\sum [w(F_o^2 - F_c^2)^2] / \sum [w(F_o^2)^2]]^{1/2}$, w = 1/[σ²(F_o²) + (aP)² + bP], where P = [max(F_o² or 0) + 2(F_c²)]/3.

Table S2. Selected Bond Lengths [Å] for **1**.

Re1	C23	2.126(3)
Re1	Cl2	2.3277(10)
Re1	Cl1	2.3359(9)
Mn1	O20	1.857(2)
Mn1	O1	1.882(2)
Mn1	N2	1.973(3)
Mn1	N1	1.992(3)
Mn1	N3	2.225(3)
C23	N3	1.135(4)
O20	C20	1.329(4)
O1	C1	1.341(4)
C1	C2	1.398(5)
C1	C6	1.409(5)
C19	C18	1.373(5)
C19	C20	1.405(4)
C2	C3	1.374(5)
N2	C14	1.290(4)
N2	C11	1.507(4)
C12	C11	1.531(5)
C18	C17	1.404(5)
C20	C15	1.405(5)
C5	C4	1.376(5)
C5	C6	1.416(5)
C14	C15	1.440(5)
C11	C13	1.528(5)
C11	C8	1.562(5)
C7	N1	1.294(4)
C7	C6	1.441(5)
C15	C16	1.410(5)
N1	C8	1.501(4)
C9	C8	1.540(5)
C3	C4	1.392(5)
C10	C8	1.532(5)
C17	C16	1.372(5)
C17	C22	1.505(5)
C4	C21	1.500(5)
C24	C25	1.374(8)
C26	N5	1.280(13)
C26	C26#	1.54(2)
N4	C25	1.139(11)

-x+1,-y+1, -z+1

Table S3. Selected Angles [°] for **1**

C23*	Re1	C23	180.0	O20	C20	C19	118.0(3)
C23*	Re1	Cl2	90.38(9)	C15	C20	C19	118.1(3)
C23	Re1	Cl2	89.62(9)	C4	C5	C6	122.4(3)
Cl2	Re1	Cl2*	180.00(5)	N2	C14	C15	127.4(3)
C23*	Re1	Cl1	89.83(9)	N2	C11	C13	111.2(3)
C23	Re1	Cl1	90.16(9)	N2	C11	C12	107.6(3)
Cl2	Re1	Cl1	89.88(4)	C13	C11	C12	109.6(3)
Cl2*	Re1	Cl1	90.12(4)	N2	C11	C8	106.7(2)
Cl1	Re1	Cl1*	180.0	C13	C11	C8	110.8(3)
O20	Mn1	O1	90.77(10)	C12	C11	C8	110.9(3)
O20	Mn1	N2	94.79(10)	N1	C7	C6	125.6(3)
O1	Mn1	N2	166.59(11)	N1	C7	H7	117.2
O20	Mn1	N1	175.52(11)	C6	C7	H7	117.2
O1	Mn1	N1	91.85(11)	C20	C15	C16	119.3(3)
N2	Mn1	N1	81.88(11)	C20	C15	C14	122.9(3)
O20	Mn1	N3	90.63(10)	C16	C15	C14	117.8(3)
O1	Mn1	N3	98.75(11)	C1	C6	C5	118.9(3)
N2	Mn1	N3	93.39(11)	C1	C6	C7	123.2(3)
N1	Mn1	N3	92.56(11)	C5	C6	C7	117.7(3)
N3	C23	Re1	177.6(3)	C7	N1	C8	121.5(3)
C20	O20	Mn1	128.2(2)	C7	N1	Mn1	123.0(2)
C1	O1	Mn1	124.4(2)	C8	N1	Mn1	115.4(2)
O1	C1	C2	119.4(3)	C2	C3	C4	121.9(3)
O1	C1	C6	122.4(3)	C16	C17	C18	117.3(3)
C2	C1	C6	118.1(3)	C16	C17	C22	122.4(4)
C23	N3	Mn1	155.0(3)	C18	C17	C22	120.2(3)
C18	C19	C20	120.9(3)	C5	C4	C3	117.5(3)
C18	C19	H19	119.5	C5	C4	C21	121.7(4)
C20	C19	H19	119.5	C3	C4	C21	120.8(4)
C3	C2	C1	121.2(3)	C17	C16	C15	122.5(3)
C3	C2	H2	119.4	N1	C8	C10	106.0(3)
C1	C2	H2	119.4	N1	C8	C9	111.6(3)
C14	N2	C11	120.7(3)	C10	C8	C9	108.7(3)
C14	N2	Mn1	122.8(2)	N1	C8	C11	106.4(2)
C11	N2	Mn1	116.1(2)	C10	C8	C11	112.9(3)
C19	C18	C17	121.7(3)	C9	C8	C11	111.1(3)
O20	C20	C15	123.8(3)	N5	C26	C26 [#]	175.7(11)
				N4	C25	C24	172.6(12)

* -x, -y, -z; # -x+1,-y+1, -z+1

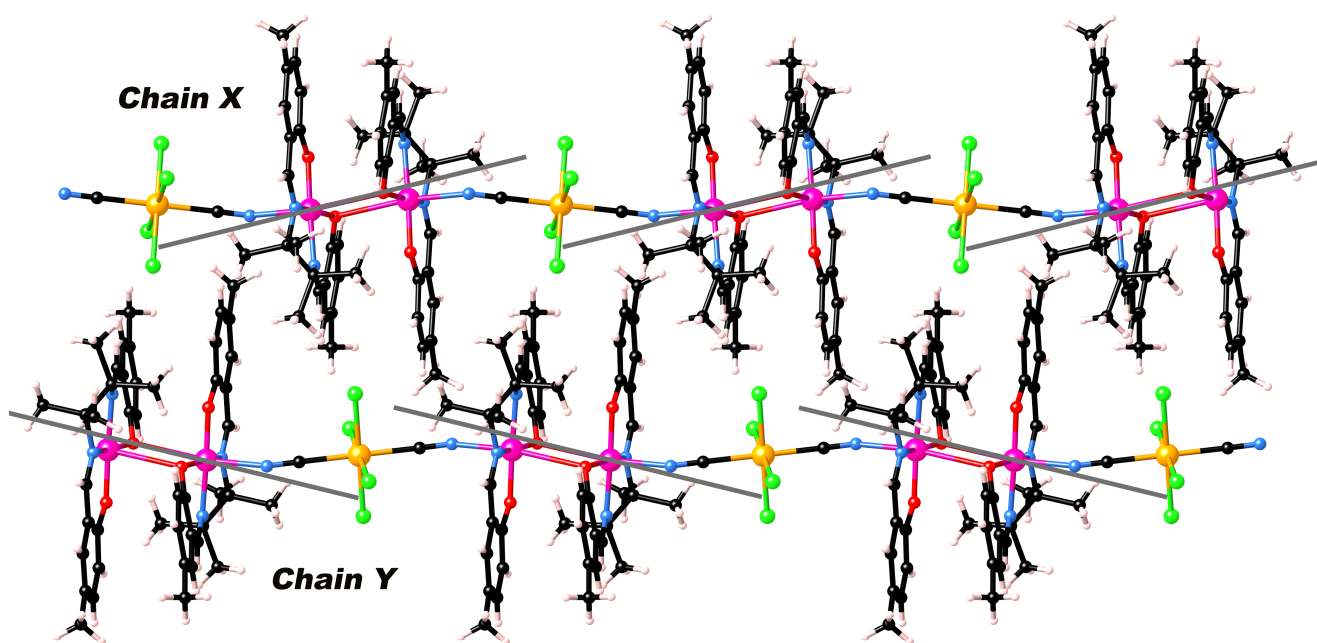


Figure S1. View emphasizing the presence and the orientation (at *ca.* 25° based on the Mn-O Jahn-Teller axes of the Mn^{III} site) of the two different chains (X and Y) present in the crystal structure of **1**. In orange, purple, pink, green, red, blue and black spheres represent the Re, Mn, H, Cl, O, N and C atoms respectively. Solvent molecules have been omitted for clarity.

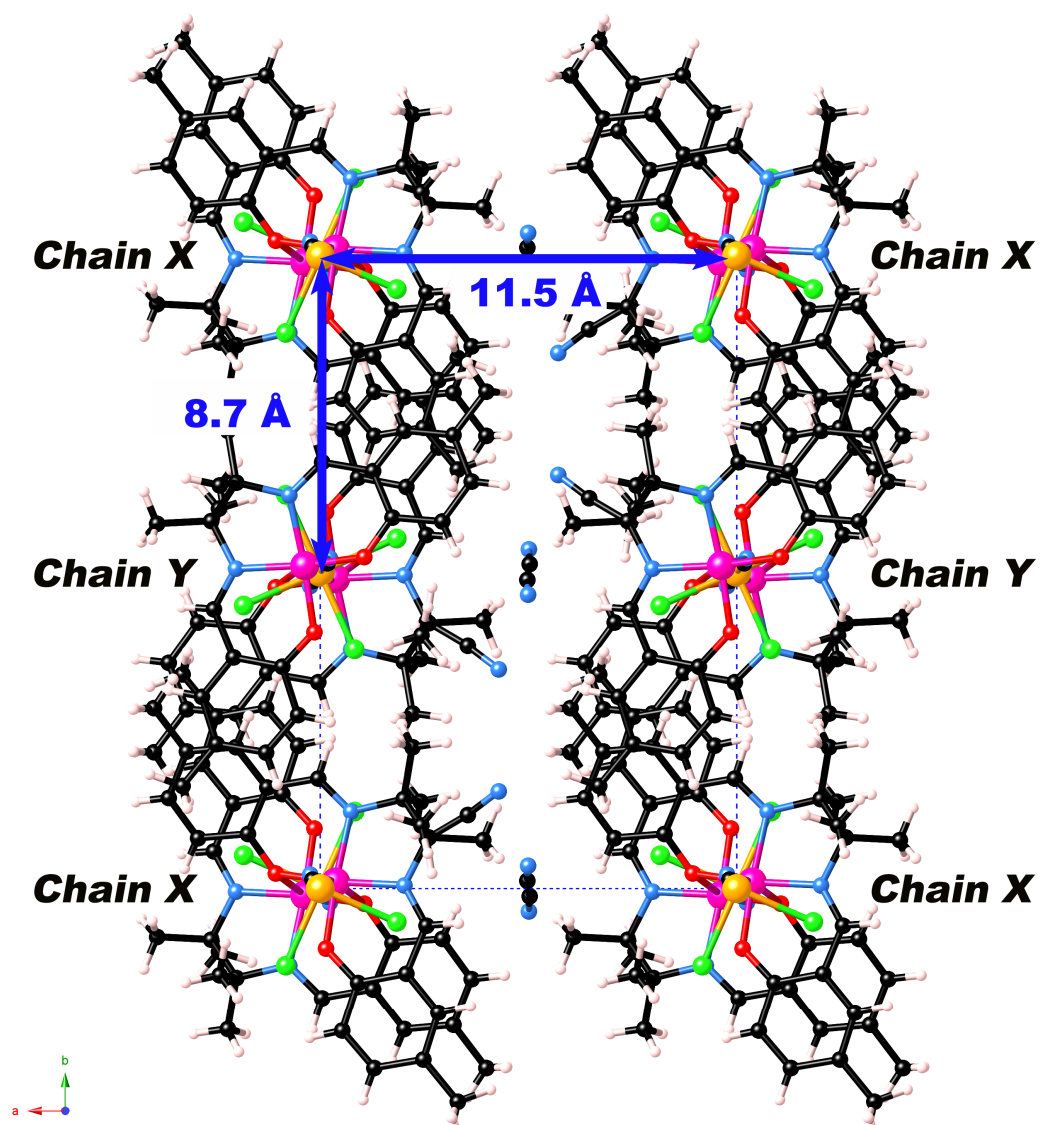


Figure S2. View of the chain (X and Y) packing in the crystal structure of **1** along the crystallographic *c* axis. In orange, purple, pink, green, red, blue and black represent the Re, Mn, H, Cl, O, N and C atoms respectively.

Details for the trinuclear 5/2-3/2-5/2 isotropic Heisenberg and mean field theoretical approaches to model the magnetic susceptibility of 1:

Compound **1** acts like a one-dimensional assembly of trinuclear ($\text{Mn}^{\text{III}}\text{-Re}^{\text{IV}}\text{-Mn}^{\text{III}}$) moieties having strong $\text{Re}^{\text{IV}}\text{-Mn}^{\text{III}}$ antiferromagnetic interactions (J , through the cyanido ligands) connected through weak ferromagnetic interactions (J' , through the double-phenoxido bridges). So at a first approximation, the magnetic susceptibility of the trinuclear $\text{Mn}^{\text{III}}\text{-Re}^{\text{IV}}\text{-Mn}^{\text{III}}$ unit should be described on the basis of the following isotropic Heisenberg Hamiltonian:

$$H = -2J(\vec{S}_{\text{Mn}1} + \vec{S}_{\text{Mn}1*}) \cdot \vec{S}_{\text{Re}1}$$

where S_i are the spin operators for each metal ion ($S_{\text{Mn}1} = S_{\text{Mn}1*} = 2$, for Mn^{III} sites; $S_{\text{Re}1} = 3/2$, Re^{IV} sites). The theoretical expression of the magnetic susceptibility can be estimated applying the van Vleck equation [J. H. van Vleck, *The Theory of Electric and Magnetic Susceptibility*, Oxford University Press, (1932)] in the weak field approximation:

$$\begin{aligned} \chi_{\text{trinuclear}} &= \frac{g^2 N \mu_B^2}{4k_B T} \left(\frac{A(J, T)}{B(J, T)} \right) \\ A &= 286 + 165 \left(e^{\frac{-3J}{k_B T}} + e^{\frac{-11J}{k_B T}} \right) + 84 \left(e^{\frac{-6J}{k_B T}} + e^{\frac{-12J}{k_B T}} + e^{\frac{-20J}{k_B T}} \right) + 35 \left(e^{\frac{-9J}{k_B T}} + e^{\frac{-13J}{k_B T}} + e^{\frac{-19J}{k_B T}} + e^{\frac{-27J}{k_B T}} \right) + 10 \left(e^{\frac{-12J}{k_B T}} + e^{\frac{-14J}{k_B T}} + e^{\frac{-18J}{k_B T}} + e^{\frac{-24J}{k_B T}} \right) + \left(e^{\frac{-17J}{k_B T}} + e^{\frac{-21J}{k_B T}} \right) \\ B &= 6 + 5 \left(e^{\frac{-3J}{k_B T}} + e^{\frac{-11J}{k_B T}} \right) + 4 \left(e^{\frac{-6J}{k_B T}} + e^{\frac{-12J}{k_B T}} + e^{\frac{-20J}{k_B T}} \right) + 3 \left(e^{\frac{-9J}{k_B T}} + e^{\frac{-13J}{k_B T}} + e^{\frac{-19J}{k_B T}} + e^{\frac{-27J}{k_B T}} \right) + 2 \left(e^{\frac{-12J}{k_B T}} + e^{\frac{-14J}{k_B T}} + e^{\frac{-18J}{k_B T}} + e^{\frac{-24J}{k_B T}} \right) + \left(e^{\frac{-17J}{k_B T}} + e^{\frac{-21J}{k_B T}} \right) \end{aligned}$$

In order to fit the low temperature χT product taking into account the magnetic coupling between trinuclear unit, J' has been introduced in the model in the frame of the mean field theory with the following definition of the susceptibility:

$$\chi = \frac{\chi_{\text{trinuclear}}}{1 - \frac{2zJ'}{Ng^2 \mu_B^2} \chi_{\text{trinuclear}}}$$

where z the number of nearest neighbors and g the average g factor of the trinuclear moiety [See for example: (a) Myers, B.E.; Berger L.; Friedberg, S. *J. Appl. Phys.* **1969**, *40*, 1149; (b) O'Connor, C. J. *Prog. Inorg. Chem.* **1982**, *29*, 203].

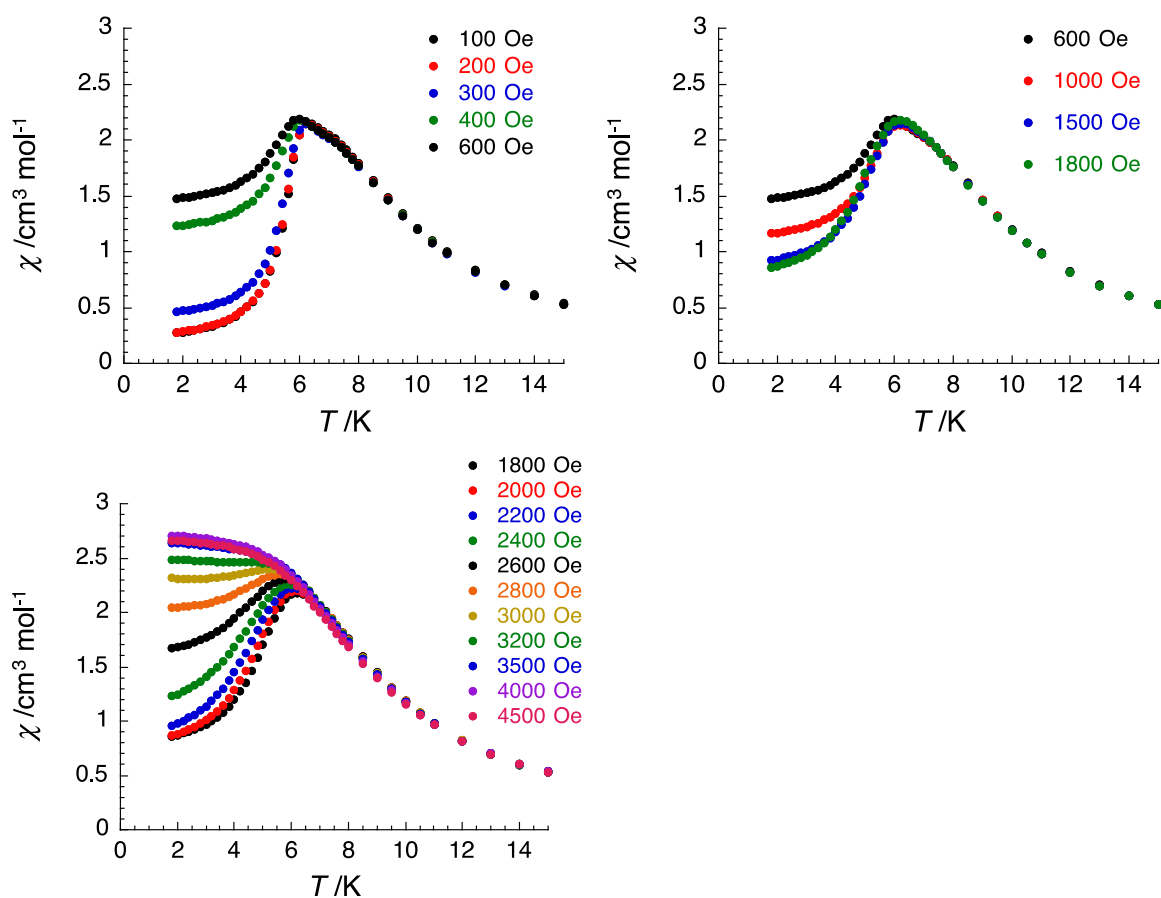


Figure S3. Temperature dependence of the molar magnetic susceptibility (where χ is equal to M/H) at different *dc* fields up to 4500 Oe between 1.83 and 15 K for a polycrystalline sample of **1**.

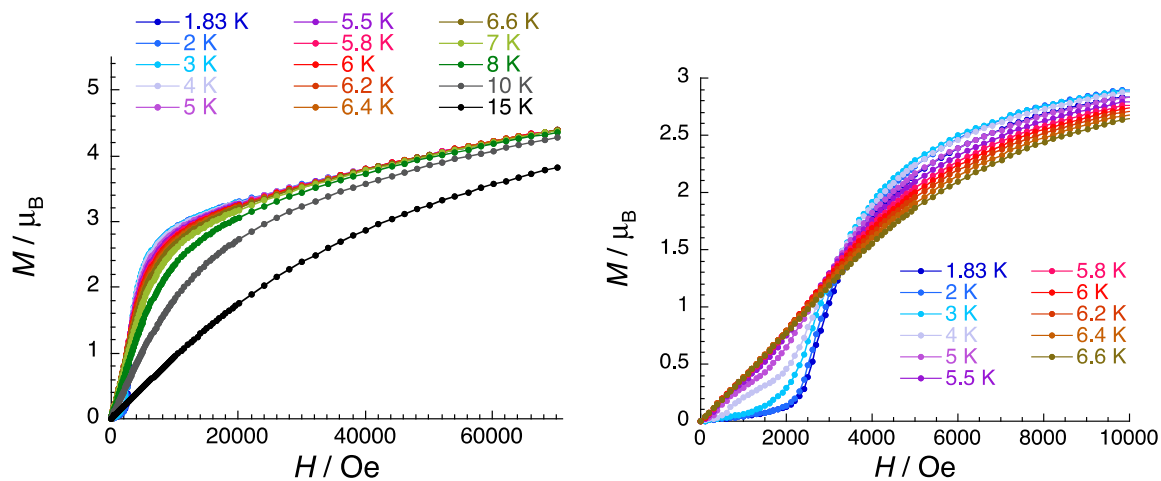


Figure S4. Field dependence of the magnetization for a polycrystalline sample of **1** between 1.8 and 15 K with sweep-rates of 100 – 200 Oe/min.

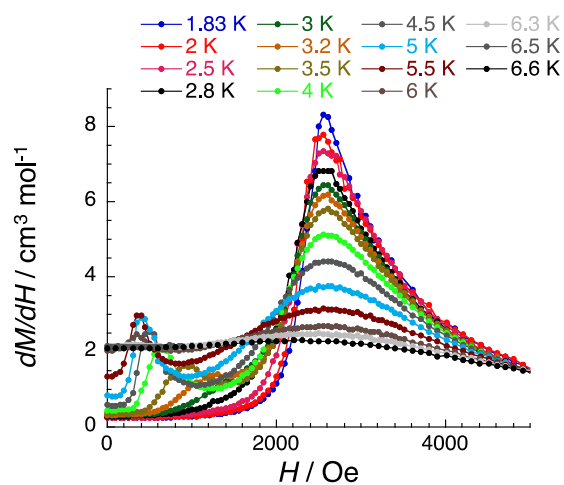


Figure S5. dM/dH vs H plots for a polycrystalline sample of **1** between 1.83 and 6.6 K with sweep-rates of 100–200 Oe/min. Solid lines are guides for the eye. Note that the first maximum observed at low field is due to the presence of M vs H hysteresis loops and thus correspond to the coercive field of the system (see Figure S6 and S7).

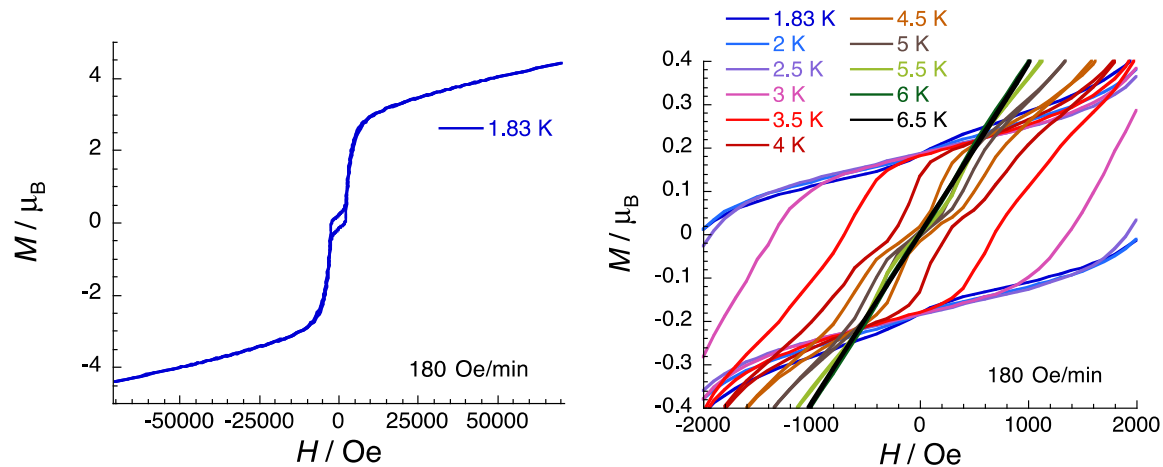


Figure S6. M vs H plots for a polycrystalline sample of **1** at 1.83 K in the -7 to 7 T field range (left) and between 1.83 and 6.5 K in the -0.2 to 0.2 T field range (right) with a sweep-rate of 180 Oe/min. The figure on the right emphasizes the presence of a hysteresis effect on the M vs H data.

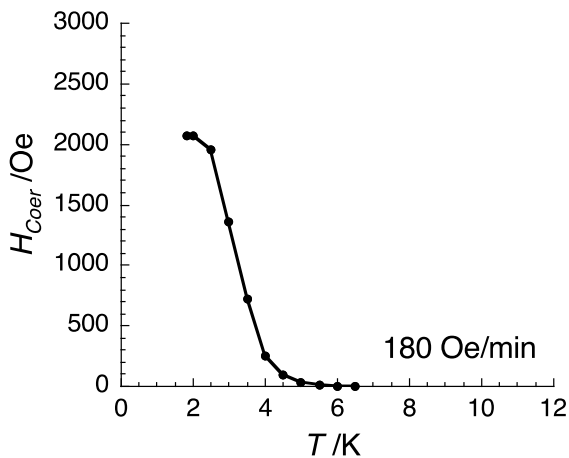


Figure S7. Temperature dependence of the coercive field deduced from Figure S6 (right part) for a polycrystalline sample of **1** with a sweep-rate of 180 Oe/min.

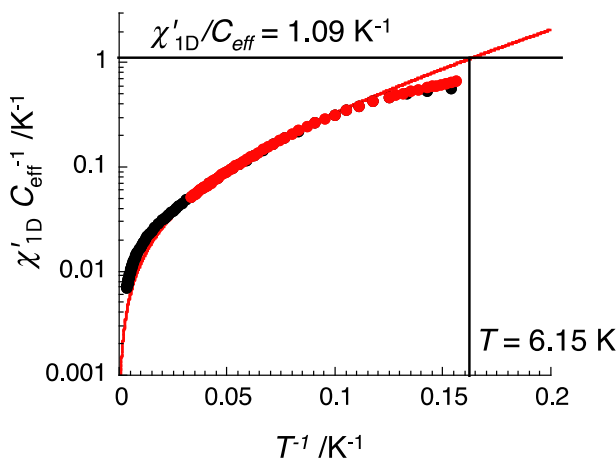


Figure S8. $\chi'_{1D} C_{eff}$ vs. $1/T$ plot (with χ'_{1D} is equal to M/H at 1000 Oe, black dots; or to the in-phase ac susceptibility at 1 Hz in zero dc field, red dots; $C_{eff} = 3.57 \text{ cm}^3 \text{K/mol}$ is the effective Curie constant deduced from the 1D fit of the data between 25 and 10 K: inset of Figure 2) where the y axis is logarithmic and the solid red line corresponds to the fit of the experimental data with the one-dimensional model between 10-25 K shown in inset of Figure 2 (see main text).

On the basis of the experimental phase diagram shown in Figure 3, the metamagnetic critical field (transition line between the canted antiferromagnetic and the paramagnetic phases) extrapolated at 0 K can be estimated at ca. 2600 Oe. This field is the magnetic field necessary to overcome the inter-chain

interactions, J_{perp} . Therefore it can be easily deduced equalizing the interaction and the Zeeman energies: $2z|J_{\text{perp}}|S_T^2/k_B = g\mu_B H_{\text{CT}}/k_B = 0.92 \text{ K}$ and thus $zJ_{\text{perp}}/k_B = -0.074 \text{ K}$.

Considering a one-dimension model of anisotropic S_T spins in the Ising limit ($|D/J| > 4/3$), the normalized susceptibility obeys the following relation: $\chi'^{\text{1D}}/C_{\text{eff}} = (1/T) \exp(\Delta_\xi/k_B T)$ where C_{eff} is the Curie constant of this model and Δ_ξ is the energy to create domain walls along the chain. The interchain magnetic interaction can be introduced in this model using the mean-field approximation and thus the resulting staggered magnetic susceptibility can be written: $\chi_{\text{AF}} = \chi'^{\text{1D}} / (1 - 2z|J_{\text{perp}}|S_T^2 \chi'^{\text{1D}}/C_{\text{eff}} k_B)$. The critical temperature of this model is obtained for the divergence of this susceptibility and thus for $2z|J_{\text{perp}}|S_T^2 \chi'^{\text{1D}}/C_{\text{eff}} k_B = 1$. This relation can be used to estimate the theoretical transition temperature of the present system considering the interchain interaction energy, $2z|J_{\text{perp}}|S_T^2/k_B = 0.92 \text{ K}$, deduced from the metamagnetic critical field and the one-dimensional model used to fit the experimental data between 25 and 10 K: $\chi'^{\text{1D}} = (C_{\text{eff}}/T) \exp(\Delta_\xi/k_B T)$ (red line in inset of figure 2 or in Figure S8; with $C_{\text{eff}} = 3.57 \text{ cm}^3 \text{K/mol}$ and $\Delta_\xi/k_B = 11.6 \text{ K}$). Graphically as shown in Figure S8, the critical temperature is obtained when $\chi'^{\text{1D}}/C_{\text{eff}} = k_B/(2z|J_{\text{perp}}|S_T^2) = 1.09 \text{ K}^{-1}$ and thus the critical temperature of the system is estimated at 6.15 K in excellent agreement with the experimental value of 6.2 K.

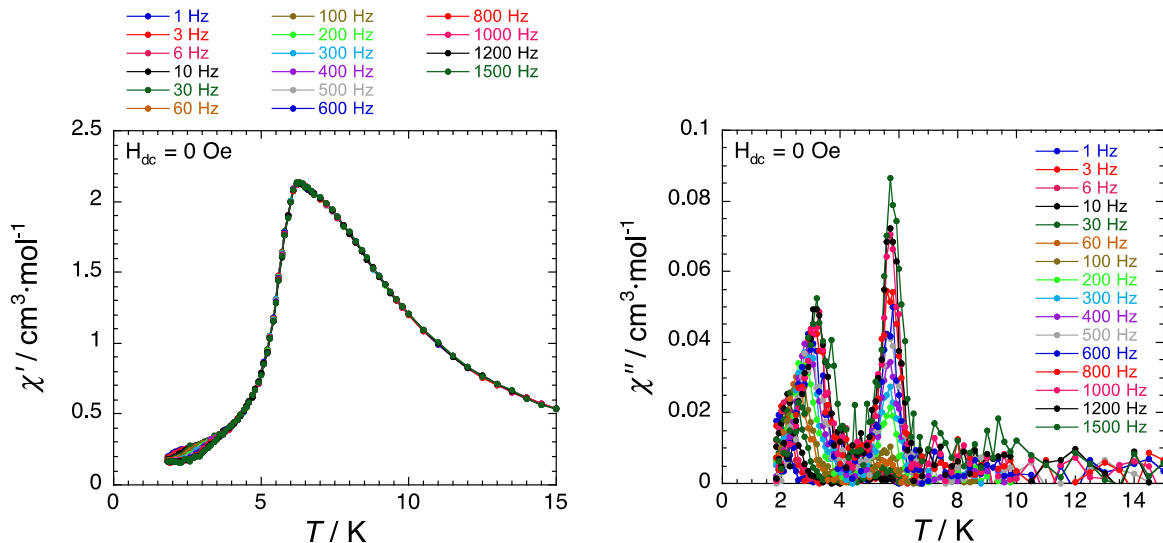


Figure S9. Temperature dependence of the real (χ') and imaginary (χ'') parts of the ac susceptibility for a polycrystalline sample of **1** in zero dc -field at different ac frequency between 1 and 1500 Hz and with a 3 Oe ac field. Solid lines are guides.

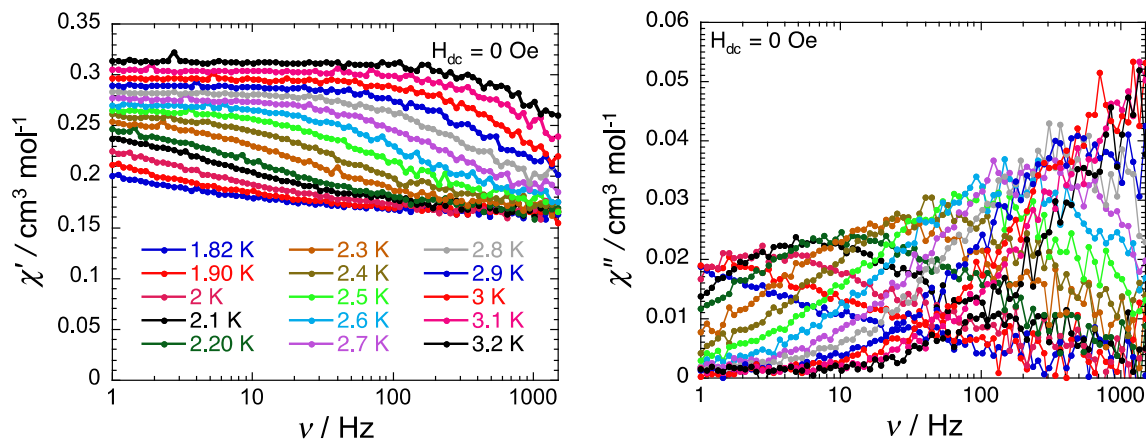


Figure S10. Frequency dependence of the real (χ' , left) and imaginary (χ'' , right) parts of the *ac* susceptibility for a polycrystalline sample of **1** in zero *dc* field at different temperatures between 1.82 and 3.2 K. Solid lines are guides.

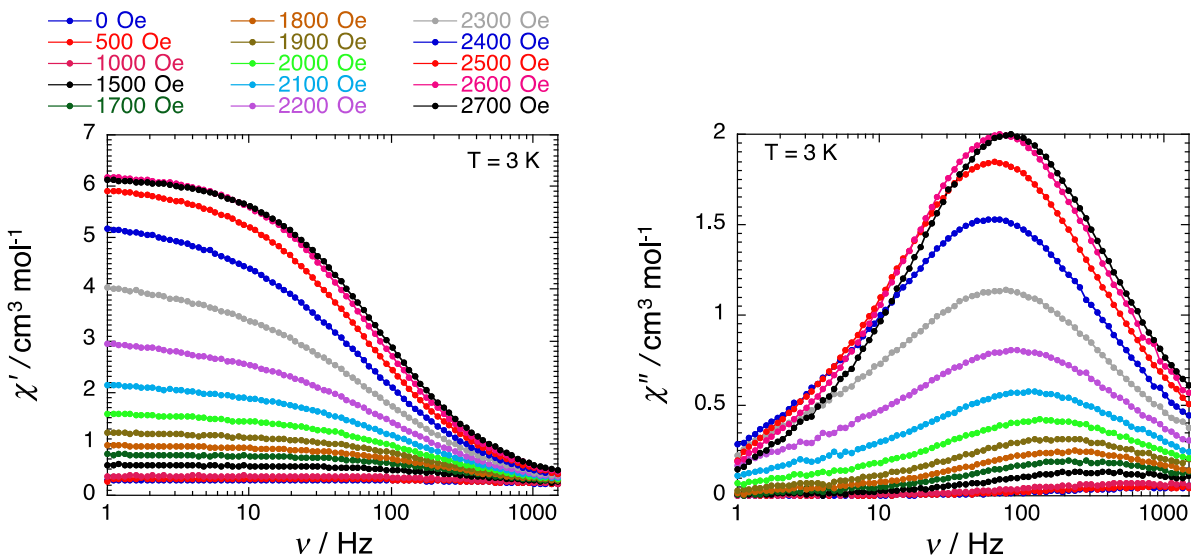


Figure S11. Frequency dependence of the real (χ' , left) and imaginary (χ'' , right) parts of the *ac* susceptibility for a polycrystalline sample of **1** at 3 K at different *dc*-field between 0 and 2700 Oe. Solid lines are guides.

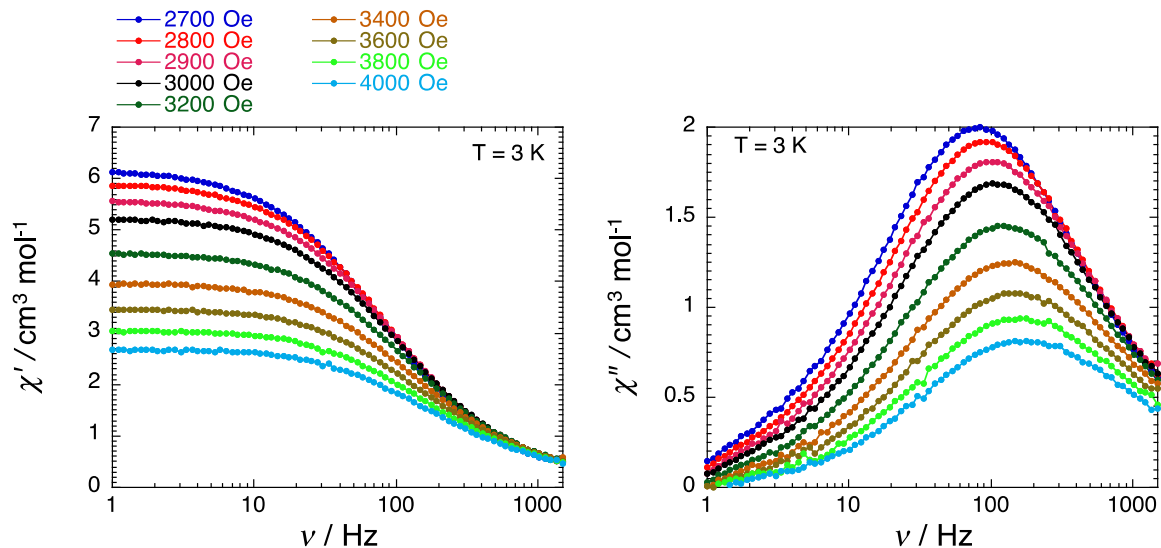


Figure S12. Frequency dependence of the real (χ' , left) and imaginary (χ'' , right) parts of the *ac* susceptibility for a polycrystalline sample of **1** at 3 K at different *dc*-field between 2700 and 4000 Oe. Solid lines are guides.

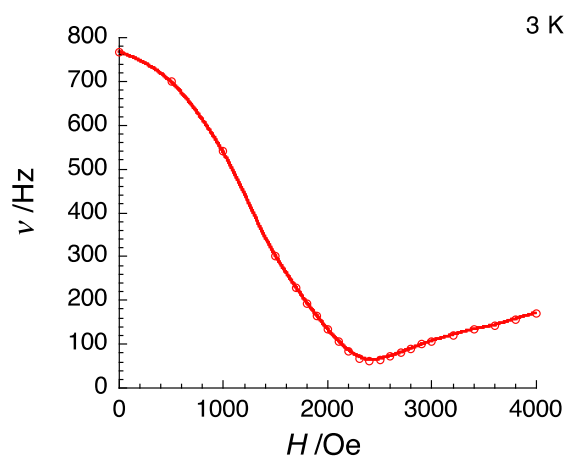


Figure S13. Field dependence of the characteristic relaxation frequency of the magnetization as a function of the applied field in **1** at 3 K. This plot is deduced from Figures 11 and S12.

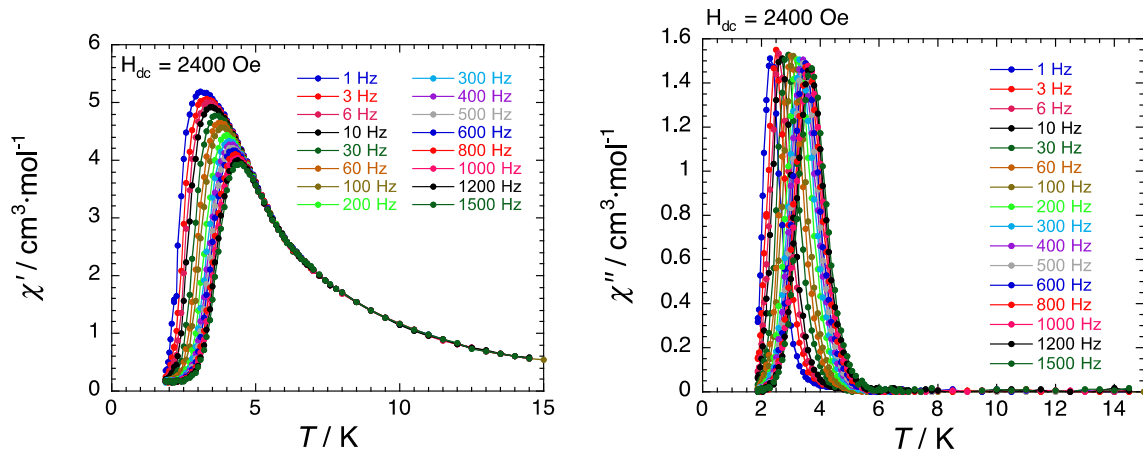


Figure S14. Temperature dependence of the real (χ') and imaginary (χ'') parts of the *ac* susceptibility for a polycrystalline sample of **1** in 2400 Oe *dc*-field at different *ac* frequency between 1 and 1500 Hz and with a 3 Oe *ac* field. Solid lines are guides.

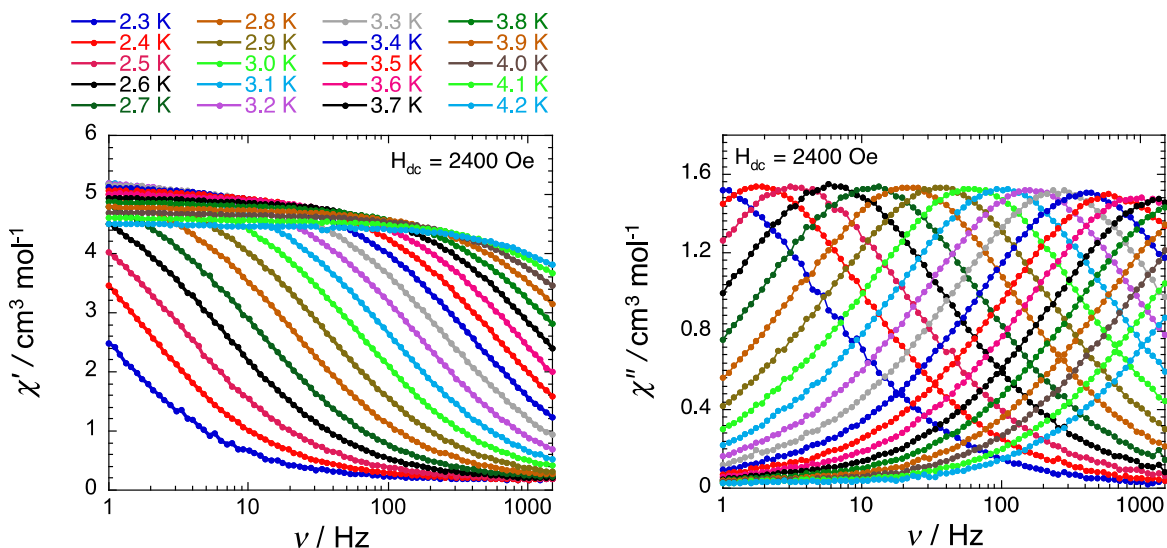


Figure S15. Frequency dependence of the real (χ' , left) and imaginary (χ'' , right) parts of the *ac* susceptibility for a polycrystalline sample of **1** in 2400 Oe *dc*-field at different temperatures between 2.3 and 4.2 K. Solid lines are guides.